Advance Publication

IEEJ Journal of Industry Applications
J-STAGE Advance published date : June 13, 2025
DOI : 10.1541/ieejjia.25000231

Paper

Current Source Inverter-Supplied PMSM Drive System for DC Machine-Like Operation

Spasoje Mirić[*,a] Non-member, Predrag Pejović[**] Non-member
Takanobu Ohno[*] Member, Michael Haider[***] Non-member

Current source inverters (CSIs) offer advantages over voltage source inverters (VSIs) in drive systems, particularly for motor windings. CSIs feature integrated output capacitors that provide smooth voltages, mitigating issues such as interturn overvoltages, insulation degradation, bearing currents, and electromagnetic interference. Recent advancements in monolithic bidirectional switches have further enhanced their appeal. However, the complexity of CSI modulation and control limits their adoption compared to VSIs, as engineers are more familiar with PWM techniques for VSIs. To address this, we propose the *Equivalent DC Machine* (E-DCM) concept, wherein the CSI operates in an open loop with a fixed modulation index, allowing direct torque control of the PMSM through the DC link current. This enables the CSI-supplied PMSM to emulate the behavior of a traditional DC machine, simplifying control while avoiding commutation and maintenance issues. The E-DCM concept is validated through transient time-domain simulations, demonstrating its DC machine-like speed-torque characteristics and effective speed control during acceleration from zero to nominal speed.

Keywords: Current Source Inverter, DC Machine, Drive Systems, PMSM, Speed-Torque Characteristics, Torque Control

1. Introduction

In three-phase variable speed drive systems, voltage source inverters (VSIs) are commonly used to supply motors(2)(3). Typically, VSIs directly connect to the motor windings, meaning the motor winding is wired to the switching node of the VSI bridge leg. Due to this direct connection, the motor windings are exposed to square-wave voltages, which can lead to several issues, including interturn overvoltages that can reach up to twice the DC link voltage(4), harmonic losses caused by high-frequency components in the stator current(5), bearing currents(6), electromagnetic interference (EMI)(7), and insulation aging due to high $\mathrm{d}v/\mathrm{d}t$(8). These challenges have become even more pronounced with the transition from IGBTs to wide bandgap (WBG) devices, due to the significantly higher switching speeds. To address these issues in VSIs, solutions like $\mathrm{d}v/\mathrm{d}t$ filters(9), or full sine wave filters have been proposed(10)(11). However, these solutions increase the size and complexity of VSIs, thereby diminishing some of the advantages of WBGs in drive system applications.

In contrast to VSIs, current source inverters (CSIs) inherently provide smooth voltages at the motor terminals due to the output capacitors, which are integral to the CSI design. These smooth voltages eliminate typical issues in VSIs associated with high-frequency switching and pulsed voltage. For example, due to smooth voltages at the motor windings, there are no interturn overvoltages. Therefore, CSIs allow for thinner interturn insulation, which improves the slot fill factor and, consequently, the machine's power density(12). Moreover, the boost capability of CSIs makes them well-suited for wide voltage ranges, supporting wide speed operation of motors, and positioning them as an excellent choice for high-speed machines(13). Additionally, CSIs are strong candidates for motor-inverter integration, as they feature a DC-link inductor instead of a DC-link capacitor that is typically electrolytic or film type in VSIs, making them more robust and capable of withstanding higher temperatures(14). In this high-temperature aspect, it should be noted that CSI output capacitors have a lower capacitance value compared to the DC link capacitors in VSIs and can be implemented using ceramic capacitors, which are well-suited for high-temperature applications.

One disadvantage of CSIs compared to VSIs is that they require switches capable of blocking voltage and current in both directions. Traditionally, this can be achieved by connecting a MOSFET and a diode in anti-series for two-quadrant operation or by connecting two MOSFETs in anti-series for four-quadrant operation. As a result, a three-phase CSI with a four-quadrant operation requires a total of 12 MOSFETs. This complexity has historically made three-phase CSIs less commonly used in industry compared to three-phase VSIs, which only require 6 MOSFETs. However, recent advancements in semiconductor technology have introduced the monolithic bidirectional switch (MBDS), based on GaN technology(15), which can block voltage and current in both directions. This

This paper is based on Reference(1) , which published in ICEMS 2024 ©2024 IEEJ.
[a] Correspondence to: Spasoje Mirić.
E-mail: spasoje.miric@uibk.ac.at
[*] Institute for Mechatronics, University of Innsbruck
Technikerstr. 13a, 6020 Innsbruck, Austria
[**] Faculty of Electrical Engineering, University of Belgrade
Bulevar Kralja Aleksandra 73, 11120 Belgrade, Serbia.
[***] Independent Researcher, Bern, Switzerland.

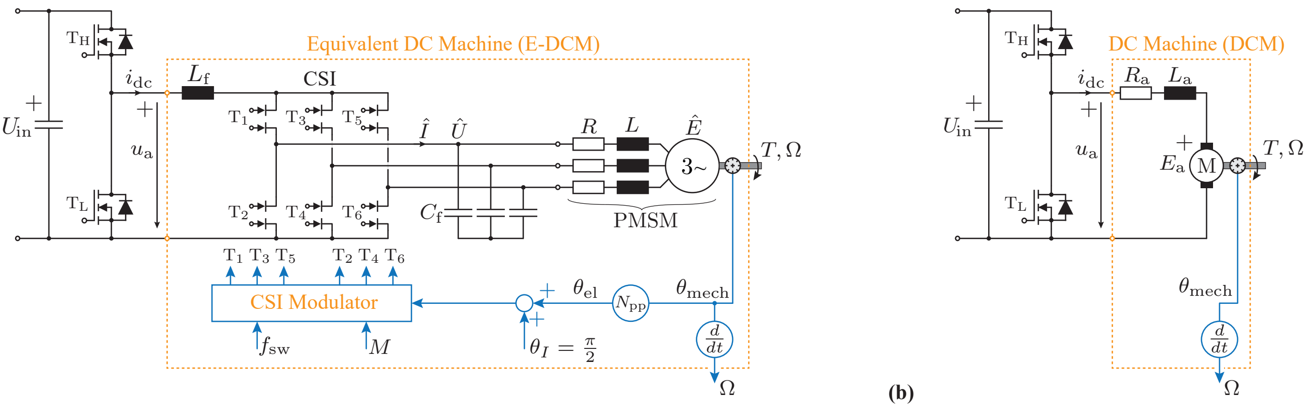

Figure 1 Comparison of the Proposed Equivalent DC Machine (E-DCM) Concept to the real DC Machine: **(a)** CSI-supplied PMSM with a constant modulation index (M), demonstrating equivalence to a DC machine from the DC side perspective of the CSI. **(b)** Representation of a real DC machine, including armature resistance, inductance, and back EMF.

allows a three-phase CSI to be realized with just 6 MBDSs. These advancements have renewed interest in CSIs for industrial applications, which is quite beneficial as CSIs can effectively address many high-frequency issues present in VSIs.

Another disadvantage of CSIs compared to VSIs is that CSIs require an input converter to regulate the DC link current, such as a CSI rectifier supplied by the power grid(16), or an input buck converter when supplied by a DC voltage source(13). However, in certain applications, a VSI system also requires an additional input converter. For instance, in fuel cell applications, due to large voltage variations, a VSI needs an input boost converter to adjust the DC link voltage(13). In this case, the input converter is not a disadvantage for a CSI as the bridge leg used for the boost converter can be repurposed as a buck leg to control the DC link current for the CSI, as shown in **Fig. 1(a)**, resulting in similar realization effort for VSI and CSI. It is worth noting that some CSI drive systems attempt to bypass the need for an input converter by directly controlling the DC link current through the CSI itself. However, this approach requires an additional leg to perform short-circuit operations(17).

One challenge hindering the widespread adoption of such CSI drive systems in the industry is their complex control structure, which typically involves coupled control between the input buck stage and the CSI. Moreover, engineers are far more familiar with controlling and modulating VSIs, which are widely used, compared to CSIs, which have been less popular due to the lack of suitable switches (such as the now available MBDS). Therefore, to simplify the control of the CSI drive system and decouple the connection between the buck converter and the CSI, this paper proposes an open-loop control for the CSI, like depicted in **Fig. 1(a)**. In this approach, the CSI modulation index is fixed at a constant value $m = M$, and the current angle is set to a constant value $\theta_i = \theta_I = \frac{\pi}{2}$ for positive torque (or $-\frac{\pi}{2}$ for negative torque). The key advantage of this system is that the user does not need to manage the CSI control, as in this case, torque control can be achieved directly by regulating the DC link current, i.e., with m and θ_i values fixed, the PMSM torque T becomes directly proportional to the DC link current i_{dc}. Ultimately, this approach makes CSI-supplied PMSM behave like a DC machine depicted in **Fig. 1(b)**. To further simplify practical implementations, a dedicated IC (based on this approach) can be designed to handle CSI open-loop control and modulation, making the use of CSI drive systems exceptionally straightforward for the users.

The paper is structured as follows. To better understand the proposed open-loop operation of the CSI, we derive the DC side equivalent circuit of the CSI in **Sec. 2**. This is particularly important because, with the input buck converter, we now directly control the PMSM torque. In **Sec. 3**, the open-loop operation of CSI is shown to exhibit behavior equivalent to that of a DC machine by deriving a DC-side speed torque characteristic whose properties are identical to those of a separately excited DC machine. Therefore, we refer to this control concept as the *Equivalent DC Machine* (E-DCM) concept. In **Sec. 4**, we discuss the DC-side torque constant for the E-DCM control concept. **Sec. 5** presents verification results that fully validate the E-DCM concept, and **Sec. 7** concludes the paper.

In **Sec. 3**, the open-loop operation of CSI is shown to exhibit behavior equivalent to that of a DC machine by deriving a DC-side speed torque characteristic whose properties are identical to those of a separately excited DC machine.

2. DC-Side Equivalent Circuit of CSI

To derive the DC-side equivalent circuit of a CSI, we consider the schematic shown in **Fig. 2(a)**, where a DC link current is impressed on the DC side, resulting in the voltage u_b at the input of the CSI. It is important to note that u_b is pulsed voltage in reality, but our DC-side equivalent circuit will model its average value $\overline{u}_b$, which can be used for tasks such as controller design.

On the output side of the CSI, we assume a PMSM connected with typical parameters, including winding resistance R, phase inductance L, and back EMF voltages e_1, e_2, and e_3. With the advent of new MBDS technology, CSIs can now be built to support high switching frequencies. This allows for the use of low-capacitance output capacitors C_f, which has the advantage of minimizing the capacitor current component at the fundamental frequency. As a result, we can neglect capacitors in our analysis as it covers only the fundamental frequency range, resulting in the justified approximation

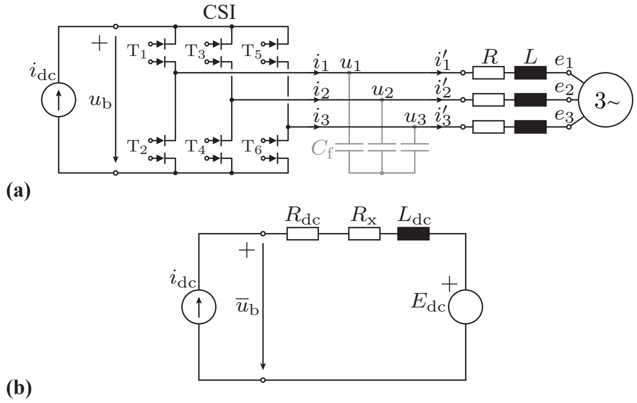

Figure 2 **(a)** Circuit schematic that is used for derivation of the DC-side equivalent circuit of a CSI with a symmetrical three-phase load (PMSM). Capacitors are shown in gray as their impact is neglected. **(b)** Resulting DC side equivalent circuit considering a switching frequency averaged model, i.e., $\overline{u}_{\mathrm{b}}$ being the local average of u_{b}.

$i_1 \approx i_1'$, $i_2 \approx i_2'$, and $i_3 \approx i_3'$.

The impressed DC link current i_{dc}, combined with the modulation index of the CSI m, determines the peak of the output current as $\hat{I} = m\, i_{\mathrm{dc}}$. Depending on the current angle θ_i, the instantaneous values can be obtained as

$$
\begin{aligned}
i_1 &= m\, i_{\mathrm{dc}} \cos(\theta_{\mathrm{el}} + \theta_i) \\
i_2 &= m\, i_{\mathrm{dc}} \cos(\theta_{\mathrm{el}} + \theta_i - \frac{2\pi}{3}), \\
i_3 &= m\, i_{\mathrm{dc}} \cos(\theta_{\mathrm{el}} + \theta_i + \frac{2\pi}{3})
\end{aligned}
\quad \cdots\cdots (1)
$$

where θ_{el} is the electrical flux angle, and θ_i is the current angle, i.e., a phase shift of the current with respect to the flux linkage of the PMSM, see **Fig. 1**. As mentioned, we neglect the C_{f} currents, which leads to the following voltage equations for the AC side:

$$
\begin{aligned}
u_1 &= R\, i_1 + L\, \frac{\mathrm{d}i_1}{\mathrm{d}t} + e_1 \\
u_2 &= R\, i_2 + L\, \frac{\mathrm{d}i_2}{\mathrm{d}t} + e_2, \\
u_3 &= R\, i_3 + L\, \frac{\mathrm{d}i_3}{\mathrm{d}t} + e_3
\end{aligned}
\quad \cdots\cdots (2)
$$

where the PMSM back EMFs are the time derivatives of the flux linkages, i.e., $e_1 = \frac{\mathrm{d}\psi_1}{\mathrm{d}t}$, $e_2 = \frac{\mathrm{d}\psi_2}{\mathrm{d}t}$, and $e_3 = \frac{\mathrm{d}\psi_3}{\mathrm{d}t}$. It should be noted that the per-phase inductance L represents the total inductance of each phase, including both the self-inductance and the mutual inductance between phases. Additionally, equation (2) does not account for interior PMSMs, which will be addressed in future work. The flux linkages are equal to

$$
\begin{aligned}
\psi_1 &= \hat{\Psi} \cos(\theta_{\mathrm{el}}) \\
\psi_2 &= \hat{\Psi} \cos(\theta_{\mathrm{el}} - \frac{2\pi}{3}), \\
\psi_3 &= \hat{\Psi} \cos(\theta_{\mathrm{el}} + \frac{2\pi}{3})
\end{aligned}
\quad \cdots\cdots (3)
$$

where $\hat{\Psi}$ is the flux linkage of the PMSM, a critical parameter as it directly determines both the torque and voltage constants of the machine. Performing the time derivatives of the flux linkages in (3), we get the expressions for the back EMFs that are equal to

$$
\begin{aligned}
e_1 &= \omega \hat{\Psi} \cos(\theta_{\mathrm{el}} + \frac{\pi}{2}) \\
e_2 &= \omega \hat{\Psi} \cos(\theta_{\mathrm{el}} + \frac{\pi}{2} - \frac{2\pi}{3}), \\
e_3 &= \omega \hat{\Psi} \cos(\theta_{\mathrm{el}} + \frac{\pi}{2} + \frac{2\pi}{3})
\end{aligned}
\quad \cdots\cdots (4)
$$

where $\omega = \frac{\mathrm{d}\theta_{\mathrm{el}}}{\mathrm{d}t}$ is the electrical angular frequency, which can be a function of time, i.e., $\omega = \omega(t)$. Often, we will use the peak value of the back EMF in our analysis, denoted as $\hat{E}$, which is equal to

$$\hat{E} = \omega\, \hat{\Psi}. \quad \cdots\cdots (5)$$

At this stage, all necessary parameters have been defined to derive the averaged DC-side equivalent circuit of a three-phase CSI. The derivation is based on the power balance between the DC side and the three-phase AC side, which is guaranteed by the following equation

$$\overline{u}_{\mathrm{b}} i_{\mathrm{dc}} = u_1 i_1 + u_2 i_2 + u_3 i_3, \quad \cdots\cdots (6)$$

where the AC currents and voltages are given in (1) and (2), and we assume lossless CSI, see **Fig. 2(a)**. The DC-side equivalent circuit of a CSI that we will derive in the following is depicted in **Fig. 2(b)**.

2.1 DC-Side Equivalent Resistance Using the equation for power balance (6), and taking only the voltage drop over the resistance R in (2), we get

$$\overline{u}_{\mathrm{b}}\, i_{\mathrm{dc}} = R\,(i_1^2 + i_2^2 + i_3^2), \quad \cdots\cdots (7)$$

where by using the expressions for the AC currents (1), we get the following

$$\overline{u}_{\mathrm{b}}\, i_{\mathrm{dc}} = \frac{3}{2} R\, m^2\, i_{\mathrm{dc}}^2. \quad \cdots\cdots (8)$$

If divide both sides of (8) by i_{dc}, we get the following voltage balance equation for the DC side

$$\overline{u}_{\mathrm{b}} = \underbrace{\frac{3}{2}\, m^2\, R}_{=R_{\mathrm{dc}}}\; i_{\mathrm{dc}}, \quad \cdots\cdots (9)$$

where it is easy to recognize that the DC-side equivalent resistance R_{dc} of the AC-side resistance R is equal to $R_{\mathrm{dc}} = \frac{3}{2} m^2 R$.

2.2 DC-Side Equivalent Inductance Using (6) and taking only the voltage drop over the inductance L in (2), we get the following power balance for the inductance

$$\overline{u}_{\mathrm{b}}\, i_{\mathrm{dc}} = L\, \left(\frac{\mathrm{d}i_1}{\mathrm{d}t}\, i_1 + \frac{\mathrm{d}i_2}{\mathrm{d}t}\, i_2 + \frac{\mathrm{d}i_3}{\mathrm{d}t}\, i_3 \right). \quad \cdots\cdots (10)$$

Knowing that for any time function $f(t)$, it holds $\frac{\mathrm{d}f(t)^2}{\mathrm{d}t} = 2\, f(t) \frac{\mathrm{d}f(t)}{\mathrm{d}t}$, we can reshape (10) into the following form

$$\overline{u}_{\mathrm{b}}\, i_{\mathrm{dc}} = L\, \frac{1}{2} \left(\frac{\mathrm{d}i_1^2}{\mathrm{d}t} + \frac{\mathrm{d}i_2^2}{\mathrm{d}t} + \frac{\mathrm{d}i_3^2}{\mathrm{d}t} \right). \quad \cdots\cdots (11)$$

In (11), we can take out the time derivative in front of the brackets, resulting in the following power balance expression:

$$\overline{u}_{\mathrm{b}}\, i_{\mathrm{dc}} = L\,\frac{1}{2}\,\frac{\mathrm{d}}{\mathrm{d}t}\left(i_1^2 + i_2^2 + i_3^2\right). \quad \cdots\cdots\cdots\cdots\cdots\cdots \quad (12)$$

Using the expression for the AC currents (1), the power balance (12) can be transformed into

$$\overline{u}_{\mathrm{b}}\, i_{\mathrm{dc}} = \frac{3}{2}\,L\,\frac{1}{2}\,\frac{\mathrm{d}(m^2\, i_{\mathrm{dc}}^2)}{\mathrm{d}t}. \quad \cdots\cdots\cdots\cdots\cdots\cdots \quad (13)$$

After expanding the derivative of the product $(m^2\, i_{\mathrm{dc}}^2)$ in (13) and dividing both sides with i_{dc}, finally, we get the voltage balance from which we can deduce the DC-side equivalent parameters of an AC-side inductance L

$$\overline{u}_{\mathrm{b}} = \underbrace{\frac{3}{2}\,L\,m\frac{\mathrm{d}m}{\mathrm{d}t}}_{=R_{\mathrm{x}}}\; i_{\mathrm{dc}} + \underbrace{\frac{3}{2}\,m^2\,L}_{=L_{\mathrm{dc}}}\;\frac{\mathrm{d}i_{\mathrm{dc}}}{\mathrm{d}t}. \quad \cdots\cdots\cdots\cdots \quad (14)$$

Therefore, the AC-side inductance L is seen on the DC side as a series connection of the resistance R_{x} and the inductance L_{dc}. Interestingly, in the DC-side equivalent circuit, a resistance R_{x} appears. This resistance models the power required to increase or decrease the energy in the AC-side inductance L. Therefore, it exists only when the modulation index m is changing ($R_{\mathrm{x}} \sim \frac{\mathrm{d}m}{\mathrm{d}t}$) and it can take negative values when the modulation index m decreases.

2.3 DC-Side Equivalent Back EMF By taking only the back-EMF voltage component in (2) and applying it to (6), we get the power balance for back-EMF voltages

$$\overline{u}_{\mathrm{b}}\, i_{\mathrm{dc}} = e_1 i_1 + e_2 i_2 + e_3 i_3, \quad \cdots\cdots\cdots\cdots\cdots\cdots \quad (15)$$

which we can further expand by using the expressions for the back-EMF voltages (4) and (5), resulting in

$$\overline{u}_{\mathrm{b}}\, i_{\mathrm{dc}} = \underbrace{\frac{3}{2}\,m\,\sin\theta_i\,\hat{E}}_{=E_{\mathrm{dc}}}\; i_{\mathrm{dc}} \quad \cdots\cdots\cdots\cdots\cdots\cdots \quad (16)$$

where $E_{\mathrm{dc}} = \frac{3}{2}\,m\,\sin\theta_i\,\hat{E}$ is the DC-side equivalent back EMF. Here should be noted that the current angle θ_i suits the traditionally used dq current angle, where for the typical maximum torque per ampere, q current component $i_{\mathrm{q}} = \hat{I}\sin\theta_i$ is applied, which is equivalent to applying $\theta_i = \frac{\pi}{2}$ in the analyzed CSI, see (1) and (3).

2.4 Summary of the DC-Side Equivalent Circuit The derived DC-side equivalent circuit is depicted in **Fig. 2(b)**. The expressions for the calculations of the elements are outlined in **Fig. 3(a)**. The complete DC-side circuit including the DC link inductor L_{f} is depicted in **Fig. 3(b)**. From this circuit, we can write the DC side voltage balance equation

$$\overline{u}_{\mathrm{a}} = (R_{\mathrm{dc}} + R_{\mathrm{x}})i_{\mathrm{dc}} + (L_{\mathrm{f}} + L_{\mathrm{dc}})\frac{\mathrm{d}i_{\mathrm{dc}}}{\mathrm{d}t} + E_{\mathrm{dc}}. \quad \cdots\cdots \quad (17)$$

This equation can be applied in various contexts, such as deriving DC-side transfer functions for control purposes or determining the DC-side speed-torque characteristics of the PMSM, as demonstrated in the following section.

3. DC-Side Speed-Torque Characteristic

The primary goal of this paper is to simplify the control of the CSI-based drive system by decoupling the buck converter control from the CSI control. This is achieved by running the CSI in open loop, meaning its modulation index $m = M$ and current angle $\theta_i = \theta_I$ are fixed at constant values. Therefore, this results in $\frac{\mathrm{d}m}{\mathrm{d}t} = 0$ leading to $R_{\mathrm{x}} = 0$. Consequently, the circuit from **Fig. 3(b)** becomes like the one in **Fig. 4(a)**.

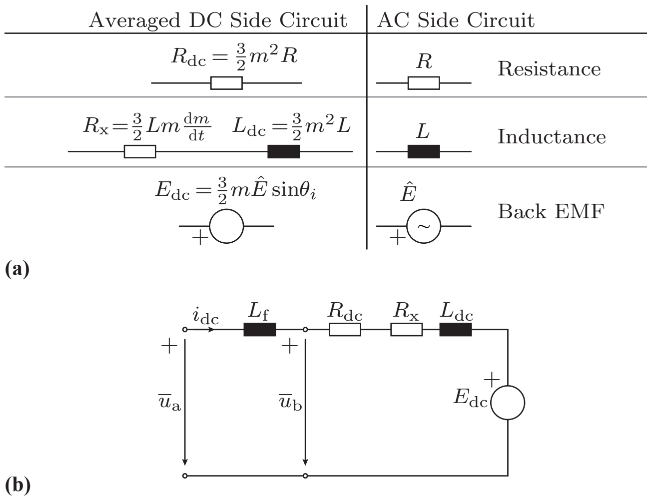

Figure 3 **(a)** Summary of the expressions for the circuit components of the DC-side equivalent circuit of a CSI–supplied PMSM. **(b)** Complete DC-side circuit equivalent including the DC link inductor L_{f}.

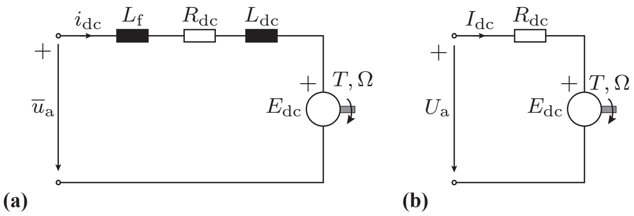

Figure 4 **(a)** DC-side equivalent circuit of the CSI–supplied PMSM considering a constant modulation index $m = M$, therefore, $R_{\mathrm{x}} = 0$, see (14). **(b)** The DC–side speed-torque characteristic can be derived from the steady-state equivalent circuit, where inductances are not considered.

In this section, we aim to explore the mechanical aspects of the drive system by deriving the equivalent DC-side speed-torque characteristics of the open-loop controlled CSI supplying the PMSM.

Speed-torque characteristics are typically derived under steady-state operating conditions. Therefore, all quantities are assumed to be in a steady state. Since we have reduced the analysis to the DC side, steady-state conditions on the DC side imply that inductances can be neglected. Additionally, to clearly indicate the steady-state assumption, all quantities are represented using uppercase letters

$$\overline{u}_{\mathrm{a}} \rightarrow U_{\mathrm{a}} \quad \text{and} \quad i_{\mathrm{dc}} \rightarrow I_{\mathrm{dc}}, \quad \cdots\cdots\cdots\cdots\cdots\cdots \quad (18)$$

and the same applies to the notation of the modulation index and the current angle

$$m \rightarrow M \quad \text{and} \quad \theta_i \rightarrow \theta_I. \quad \cdots\cdots\cdots\cdots\cdots\cdots \quad (19)$$

The steady-state circuit used for this derivation is shown in **Fig. 4(b)**, leading to the following voltage balance equation:

$$U_{\mathrm{a}} = R_{\mathrm{dc}} I_{\mathrm{dc}} + E_{\mathrm{dc}}. \tag{20}$$

To derive the speed-torque characteristics, our objective is to relate the electrical quantities in (20) to the mechanical torque T and speed Ω of the PMSM. It should be noted that for electrical angular frequency, we use ω, and for the mechanical speed, we use Ω, and they are related via number of pole pairs p as

$$\omega = p\,\Omega. \tag{21}$$

Therefore, using (4), (16), and (21), we can relate E_{dc} to the mechanical speed Ω as

$$E_{\mathrm{dc}} = \frac{3}{2} M \sin\theta_I\, p\hat{\Psi} \cdot \Omega. \tag{22}$$

For PMSMs, a torque constant k_{T} relates the torque on the shaft T and the quadrature current $i_{\mathrm{q}} = \hat{I}\sin\theta_I$ as

$$T = k_{\mathrm{T}}\, \hat{I} \sin\theta_I. \tag{23}$$

It is known that this torque constant is determined by the PMSM's flux linkage $\hat{\Psi}$ and it is equal to

$$k_{\mathrm{T}} = \frac{3}{2} p\hat{\Psi}, \tag{24}$$

which allows us to rewrite (22) into the following form

$$E_{\mathrm{dc}} = M\, \sin\theta_I\, k_{\mathrm{T}}\, \Omega. \tag{25}$$

Using (23), we can relate torque of the PMSM T to the DC link current I_{dc} as

$$T = k_{\mathrm{T}}\, I_{\mathrm{dc}}\, M \sin\theta_I, \tag{26}$$

since $\hat{I} = M\, I_{\mathrm{dc}}$. Finally, using (9), (25), and (26), we can write the voltage balance equation (20) as a function of solely CSI and PMSM parameters as

$$U_{\mathrm{a}} = M^2 \frac{3}{2} R \frac{T}{M \sin\theta_I\, k_{\mathrm{T}}} + M \sin\theta_I\, k_{\mathrm{T}}\, \Omega. \tag{27}$$

To get the DC-side speed-torque characteristic of the CSI-supplied PMSM, we need to rewrite (27) so that $\Omega = \Omega(U_{\mathrm{a}}, T)$, resulting in

$$\Omega = \frac{1}{M\, \sin\theta_I\, k_{\mathrm{T}}} U_{\mathrm{a}} - \frac{3}{2} \frac{R}{\sin^2\theta_I\, k_{\mathrm{T}}^2} T. \tag{28}$$

For the derived speed-torque characteristic (28), the no-load speed Ω_0 is obtained by assuming $T = 0$, which leads to

$$\Omega_0 = \frac{U_{\mathrm{a}}}{M\, \sin\theta_I k_{\mathrm{T}}}. \tag{29}$$

Similarly, the starting torque T_0 is obtained by solving (28) for T when $\Omega = 0$, resulting in

$$T_0 = \frac{2}{3} \frac{\sin\theta_I k_{\mathrm{T}}}{M\, R} U_{\mathrm{a}}. \tag{30}$$

The derived speed-torque characteristic (28) is depicted in **Fig. 5**. It should be noted that, compared to the traditional DC machine speed-torque characteristic, the derived one can expand the speed-torque range by reducing the CSI's modulation index M. Also, the current angle θ_I that can be used for field-weakening of the PMSM in high-speed operation makes the characteristic steeper, leading to the speed being more sensitive to the load torques. For lower speeds, this angle is kept to $\theta_I = \frac{\pi}{2}$, resulting in $\sin\theta_I = 1$. Moreover, when comparing this to the traditional DC machine characteristics, $\sin\theta_I$ has the same effect on the characteristics as the excitation flux in a DC machine, while the CSI modulation index M plays a similar role to the number of turns on the rotor in a conventional DC machine.

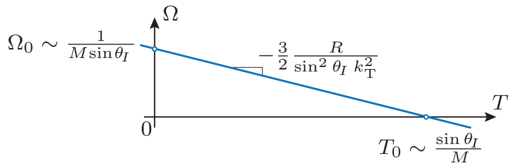

Figure 5 DC-side speed-torque characteristic of the CSI-supplied PMSM. Reducing CSI's modulation index M expands the possible speed-torque area.

4. Equivalent DC Machine (E-DCM) Concept

As demonstrated in the analysis and derivations in **Sec. 2** and **Sec. 3**, the open-loop operated CSI, where the modulation index $m = M$ and the current angle $\theta_i = \theta_I$ are fixed, behaves from the DC side like a traditional DC machine, even though in reality it is a CSI supplying a PMSM. We refer to this concept as the *Equivalent DC Machine* (E-DCM) concept. The E-DCM concept offers significant advantages by simplifying the operation of the CSI drive system, allowing direct control of the torque on the PMSM shaft through the DC link current. Thus, the E-DCM concept provides users with the simplicity and familiarity of a DC machine, while in reality, a PMSM supplied by a CSI delivers higher torque and power density compared to a traditional DC machine, without the issues of commutation or maintenance, such as replacing brushes.

When using the E-DCM concept, the torque on the PMSM shaft is determined by equation (26), which shows that the torque is directly proportional to the DC link current. While this equation is derived for steady-state conditions, it remains valid for any dynamic situation, i.e., for any value of the DC link current i_{dc}. From equation (26), we can also derive the torque constant for the E-DCM concept, given by

$$k_{\mathrm{Tdc}} = k_{\mathrm{T}}\, M\, \sin\theta_I, \tag{31}$$

which represents the proportional relationship between the PMSM torque and the DC link current, i.e., $T = k_{\mathrm{Tdc}}\, i_{\mathrm{dc}}$. Since $0 \leq M \leq 1$ and $-1 \leq \sin\theta_I \leq 1$, the DC-side equivalent torque constant is maximized if $M = 1$ and $\theta_I = \frac{\pi}{2}$, which leads to $k_{\mathrm{Tdc}} = k_{\mathrm{T}}$. Therefore, in further analysis, we will analyze E-DCM concept with

$$M = 1 \quad \text{and} \quad \theta_I = \frac{\pi}{2}, \tag{32}$$

as they maximize torque per DC link current ampere, ensuring the most efficient operation. Other parameter selections will be explored in future work.

When the E-DCM concept is applied to a CSI variable speed drive system, as shown in **Fig. 1(a)**, the drive system operates equivalently to a DC machine (see **Fig. 1(b)**). In this configuration, if the CSI drive with the E-DCM concept is connected directly to a DC voltage source, it will accelerate

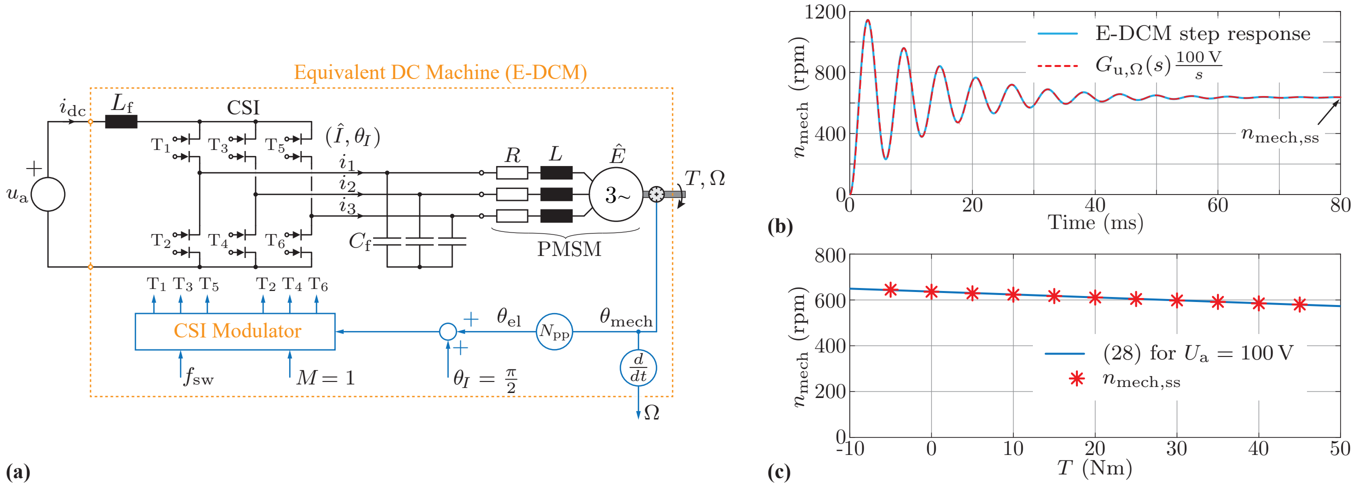

Figure 6 Voltage Step Response of the E-DCM: **(a)** Circuit schematic used for the simulation. **(b)** Step response of the mechanical speed for the voltage step of $u_a = 100\,\mathrm{V}$. **(c)** Verified DC-side speed-torque characteristic from (28).

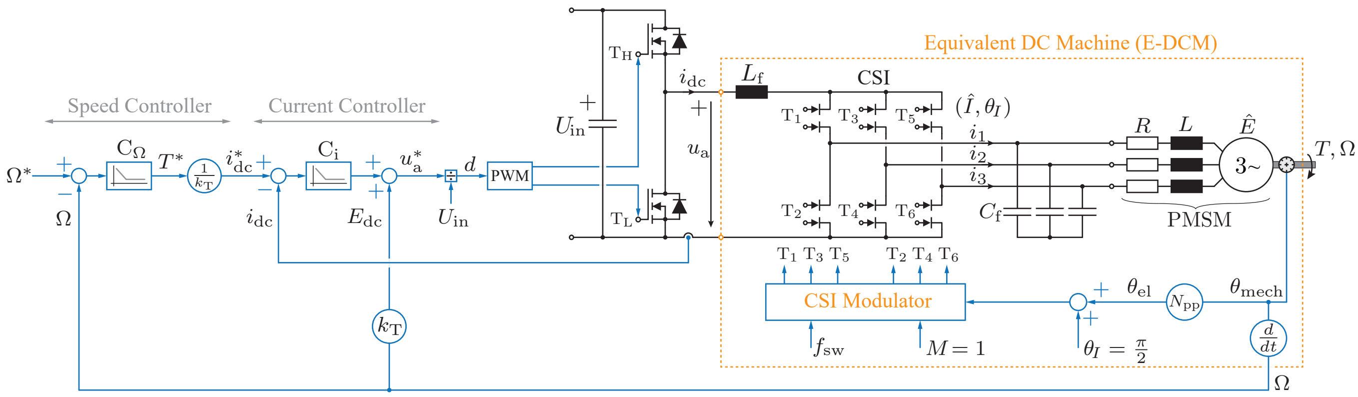

Figure 7 Proposed speed control in the CSI-supplied drive system with PMSM is achieved using open-loop CSI control. This is implemented by fixing the modulation index at $M = 1$ and the current angle at $\theta_I = \pi/2$, and with the CSI relying solely on angle information from the encoder. This open-loop control of the CSI allows speed and torque control on the PMSM shaft to be fully managed by the input buck converter. Consequently, from the perspective of the input buck converter, the DC side of the CSI behaves exactly like a DC machine, which is why we refer to this control approach as the *Equivalent DC Machine* (E-DCM). For the selected values of M and θ_I, both the torque and voltage constants on the DC side are equivalent to the PMSM's torque constant k_T, as shown in equations (25) and (26).

accordingly, like a DC machine with a separate excitation, which is analyzed in the next section and illustrated in **Fig. 6**. If we have a controlled input voltage source (e.g., a buck converter), this input buck converter takes full control of the PMSM's torque through the DC link current, mirroring the behavior of a conventional DC machine, which is also analyzed in the next section and illustrated in **Fig. 7**. Notably, the CSI operates exclusively in an open-loop configuration, requiring no user interaction. This open-loop control for the CSI can be implemented on a microcontroller, or a dedicated IC can be designed to manage both the open-loop control and modulation, further simplifying the system's operation.

5. Simulation Results

5.1 E-DCM Speed-Torque Characteristic In this section, we verify the speed-torque characteristic (28) and confirm the second-order response of the E-DCM speed (A4). For this purpose, the schematic shown in **Fig. 6(a)** is used for time-domain simulations. The CSI supplying the PMSM is directly connected to a voltage source without any DC link current control. This configuration is possible because, as demonstrated, when the CSI modulation index is fixed, the system operates under the E-DCM concept, where the CSI from its DC side behaves like a DC machine.

The step response of the mechanical speed, depicted in **Fig. 6(b)**, shows that the time-domain simulation (solid blue line) matches the theoretical step response of the speed:

$$\Omega(s) = G_{u,\Omega}(s)\, U_a(s), \quad \cdots\cdots\cdots\cdots \quad (33)$$

denoted by the dashed red line, where the transfer function $G_{u,\Omega}(s)$ is derived in **Appendix 1**. The armature voltage is a step voltage response from $U_a = 0$ to $100\,\mathrm{V}$, resulting in $U_a(s) = \frac{100\,\mathrm{V}}{s}$. The mechanical speed Ω is shown in rpm in **Fig. 6(b)** and is denoted as n_{mech}, calculated from Ω as:

$$n_{\mathrm{mech}} = \Omega\,\frac{30}{\pi}. \quad \cdots\cdots\cdots\cdots \quad (34)$$

The speed-torque characteristic (28) for $U_a = 100\,\mathrm{V}$,

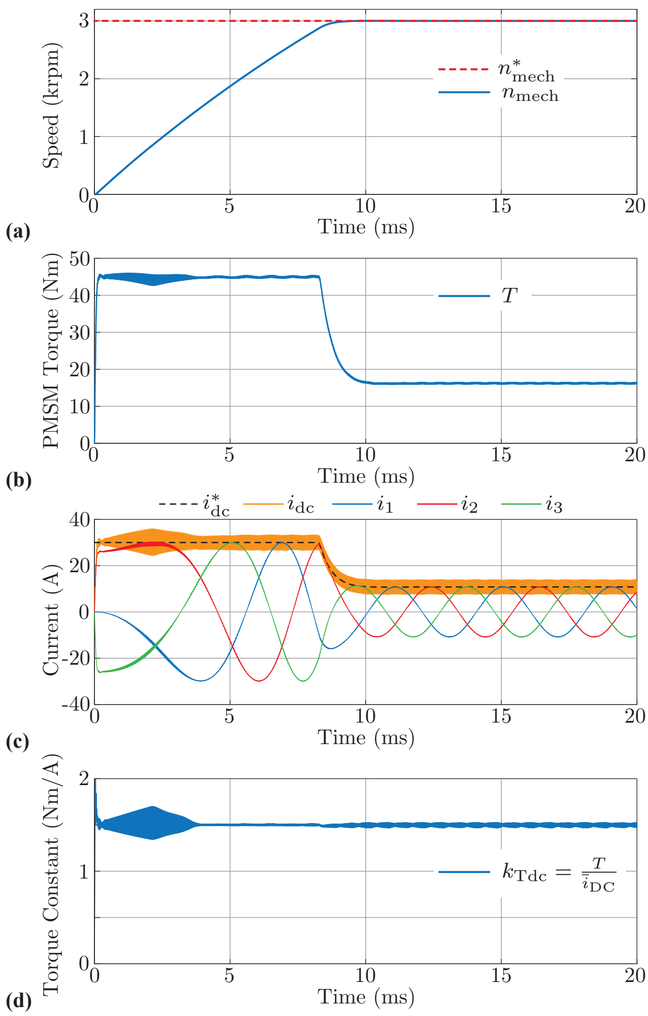

Figure 8 Simulation waveforms for the CSI drive system from **Fig. 7**, verifying E-DCM concept: **(a)** mechanical speed, **(b)** PMSM torque, **(c)** DC-link and AC currents, and **(d)** DC-side torque constant obtained by dividing the PMSM torque with the DC link current.

$M = 1$, $\sin\theta_I = 1$, $R = 0.2\,\Omega$, and $k_\mathrm{T} = \frac{3}{2}p\hat{\Psi} = 1\,\mathrm{Nm/A}$ (see **Tab. 1**) is shown as a solid blue line in **Fig. 6(c)**. The characteristic is converted to rpm using (34). Each star on the plot represents a steady-state speed value $n_{\mathrm{mech,ss}}$ achieved in the time-domain simulations, as illustrated in **Fig. 6(b)**. This result validates the derived speed-torque characteristic (28) and confirms that the E-DCM behaves like a separately excited DC machine. Specifically, the CSI supplying the PMSM with a constant modulation index and current angle exhibits DC machine-like behavior from its DC side. In the following, we will leverage the E-DCM concept for speed control applications, where both speed and torque control of the PMSM are fully managed from the DC side of the CSI.

5.2 E-DCM Speed Control To demonstrate the operation of the E-DCM concept in the CSI drive system, we implemented the configuration shown in **Fig. 7** in PLECS time-domain simulator[18], using the parameters outlined in **Tab. 1**. Note that now speed control is performed directly with the input buck converter, where the PI speed controller C_Ω produces torque reference T^* that is, based on (26), used to obtain the DC link current reference $i^*_{\mathrm{dc}} = \frac{T^*}{k_\mathrm{T}}$. The PI current controller $\mathrm{C_i}$ provides the voltage reference that should be applied over the total DC resistance R_{dc} and inductance $L_\mathrm{f} + L_{\mathrm{dc}}$, see **Fig. 4(a)**. Analog to the DC machine armature current control, we help the current controller $\mathrm{C_i}$ by adding a feedforward value of the equivalent induced back EMF that can be obtained from mechanical speed Ω measurement as $E_{\mathrm{dc}} = k_\mathrm{T}\Omega$, see (25). Finally, the reference for the DC-link ('armature') voltage u^*_a is obtained and is used to calculate the duty cycle of the input buck converter and ultimately the gate signals of $\mathrm{T_H}$ and $\mathrm{T_L}$.

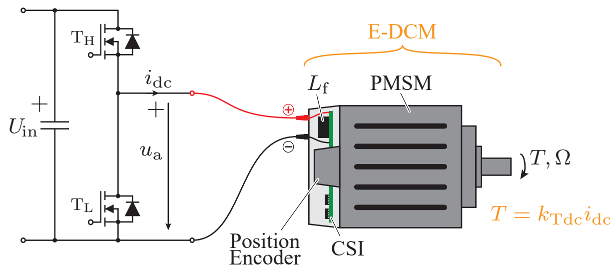

Figure 9 Conceptual 2D prototype of a PMSM-integrated CSI. When the E-DCM concept is implemented, the system operates like a traditional DC machine, with the user simply connecting the positive and negative terminals. The CSI runs in an open loop, utilizing rotor shaft information from the integrated encoder.

The time-domain simulation results are given in **Fig. 8**. The simulation waveforms show the acceleration of the PMSM from zero to nominal speed while being loaded with the torque linearly proportional to the speed $T = k_{\mathrm{fric}}\Omega$, where the friction coefficient is $k_{\mathrm{fric}} = 0.0507\,\mathrm{Nms}$, at which nominal mechanical power of 5 kW is developed for nominal mechanical speed of 3 krpm. During this speed transient, the PMSM torque reaches its maximum value of $k_\mathrm{T} \cdot I_{\mathrm{dc,max}} = 45\,\mathrm{Nm}$ before gradually reducing to its continuous nominal value, as illustrated in **Fig. 8(b)**. It should be noted that the simulation starts from a standstill at which the DC link current and output capacitor voltages are zero. Therefore, the transient with currents in **Fig. 8(c)** shows a realistic response of the system, i.e., no initial values are set to help the simulation. It can be noticed that the DC link current quickly rises to its maximum value of $I_{\mathrm{dc,max}} = 30\,\mathrm{A}$ and makes PMSM produce the maximum torque that accelerates the drive system. Once the nominal speed is achieved, the DC link current drops down to the value of 10.8 A that produces the nominal torque on the machine at a nominal speed. Furthermore, the peak of AC currents of the PMSM $\hat{I}$ is equal to the DC link current i_{dc}, which is a property of the E-DCM concept due to the fixed modulation index $M = 1$ and $\sin\theta_I = 1$. Finally, **Fig. 8(d)** illustrates the DC-side torque constant k_{Tdc}, determined by dividing the PMSM torque T by the switching-frequency-averaged DC link current $\bar{i}_{\mathrm{DC}}$. Using (24) and (31) along with the numerical values from **Tab. 1**, the DC-side torque constant is calculated as:

$$k_{\mathrm{Tdc}} = \frac{3}{2}\, p\, \hat{\Psi}\, M\, \sin\theta_I = 1.5\,\mathrm{Nm/A}, \cdots\cdots\cdots\cdots \quad (35)$$

which matches the value obtained in **Fig. 8(d)**, thereby fully validating the E-DCM concept.

Tuning PI controllers for speed-controlled drive systems is well-established in the literature, see[19]. We start the con-

Table 1 Simulation Parameters.

Parameter	Symbol	Value
Buck		
Input voltage	U_{in}	800 V
Switching frequency	$f_{sw,b}$	80 kHz
CSI		
DC link inductance	L_f	450 µH
Output capacitance	C_f	0.1 µF
Switching frequency	f_{sw}	140 kHz
Max. DC link current	$I_{dc,max}$	30 A
PMSM		
Phase resistance	R	0.2 Ω
Phase inductance	L	1 mH
Number of pole pairs	p	5
Flux linkage	$\hat{\Psi}$	0.2 Wb
Moment of inertia	J	0.001 kgm^2
Nominal mech. power	P_{mech}	5 kW
Nominal mech. speed	n_{mech}	3000 rpm
Controller gains		
C_i closed-loop bandwidth	f_{cc}	4 kHz
C_i proportional gain	K_{pc}	49 V/A
C_i integral gain	K_{ic}	10 000 V/(As)
C_Ω cross-over frequency	f_{cs}	0.8 kHz
C_Ω proportional gain	K_{ps}	3.3 sNm
C_Ω integral gain	K_{is}	3400 Nm

troller design from the inner current controller by setting first a desired C_i closed-loop bandwidth of $f_{cc} = 4$ kHz. By applying the pole-zero cancellation (PZC) method this results in analytic expressions for the PI gains: $K_{pc} = \omega_{cc}\,(L_f + L_{dc})$ and $K_{ic} = \omega_{cc}\,R_{dc}$, where $\omega_{cc} = 2\pi f_{cc}$. Tuning the current controller in this way results in a closed-loop transfer function $\frac{\omega_{cc}}{s+\omega_{cc}}$ that is a first-order. The outer speed controller is tuned using the so-called symmetrical optimum, where the speed-cross-over frequency $f_{cs} = 0.8$ kHz is typically chosen to be five times lower than the current closed-loop bandwidth, i.e, $f_{cs} = \frac{f_{cc}}{5}$. The zero of the PI speed controller C_Ω needs to be five times lower than the speed cross-over frequency $f_{pis} = \frac{f_{cs}}{5}$ to ensure the open-loop transfer function pass through 0 dB with −20 dB/decade. This finally results in the analytic expressions for the speed-controller gains: $K_{ps} = \frac{J\,\omega_{cs}}{k_T}$ and $K_{is} = \omega_{pis}\,K_{ps}$, where $\omega_{cs} = 2\pi f_{cs}$ and $\omega_{pis} = 2\pi f_{pis}$. Finally, the gain values of both controllers are summarized in **Tab. 1**.

A conceptual 2D prototype of the CSI-supplied PMSM that uses the proposed E-DCM control concept is illustrated in **Fig. 9**. This integrated drive consists of a DC link inductor L_f, a CSI, and a position encoder integrated into the casing of a PMSM, with the CSI operated as shown in **Fig. 7**. To run this motor-integrated drive system, the user simply connects the positive and negative terminals, as it functions like a DC machine, but in reality, CSI-supplied PMSM is operated.

6. Low-Power Hardware Verification

In this section, we present the hardware verification of the E-DCM concept. As discussed in the previous section, the ultimate goal is to integrate the CSI into the PMSM. However, at this stage, we use a simplified, scaled-down hardware setup to validate the E-DCM concept and verify the key waveforms, which is an essential step prior to full integration. Therefore, the parameters listed in **Tab. 1** do not apply to the hardware verification, and the relevant parameters for the experimental setup will be clarified in this section. This low-power configuration allows for practical testing of the control strategy and system behavior.

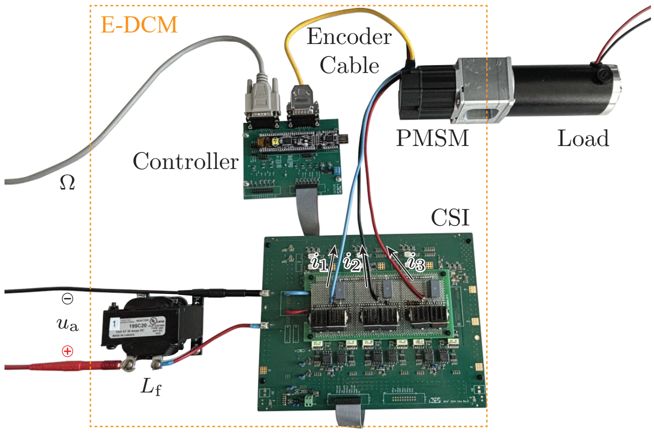

Figure 10 The hardware demonstrator used to validate the E-DCM concept, with further details about PMSM available in[20].

The experimental setup is shown in **Fig. 10** and consists of the main E-DCM drive components: a PMSM with encoder, a CSI, a controller, and a controller board. The PMSM is mechanically coupled to a DC generator, which is connected to an external resistor for power dissipation. The E-DCM setup is powered by a laboratory DC voltage supply, which regulates the DC link current to a desired value, which directly generates the torque on the PMSM shaft.

The CSI in **Fig. 10** features a DC link inductance of 1 mH and utilizes 650 V SiC MOSFETs in a TO-247-3 package, along with 650 V SiC diodes. The controller PCB is built around the CY8CKIT-059 PSoC 5LP, integrated into a custom-designed board that includes connectors for both the PMSM encoder and the CSI gate signals. Based on the rotor position detected by the encoder, the CSI modulation method described in[21] is implemented on the PSoC, with a fixed modulation index of $M = 1$ and a current angle of $\theta_I = \pi/2$. The PSoC generates the appropriate gate signals to drive the CSI. The system is powered by a laboratory DC power supply, which provides the input voltage u_a and is used to regulate the DC link current i_{dc}, thereby controlling the torque applied to the PMSM shaft. The PMSM[20] has maximum ratings of 28 V_{peak} phase-to-phase, 7 A_{rms}, and 6000 rpm, while the load motor is rated at 36 V_{dc}, 4 A_{dc}, and 3600 rpm. An external variable power resistor is connected to the DC motor to serve as a load. By adjusting the resistance value, the desired load level can be set, allowing the DC machine to operate in generator mode.

The measurements verifying the E-DCM concept are presented in **Fig. 11**. In **Fig. 11(a)**, a start-up transient from standstill to 1600 rpm is shown. This transient is achieved using a laboratory power supply operating in current control mode to supply the DC side, i.e., to provide the voltage u_a. The power supply voltage is set to $U_a = 10.8$ V—the steady-state value required to reach a rotational speed of 1600 rpm with a DC link current of 3 A. The current limit is set to 6 A.

Before the power supply is enabled, the CSI modulation is already active with a fixed modulation index of $M = 1$. Upon powering the system, the DC link current initially hits the current limit of 6 A, as there is no initial rotor speed

(a)

(b)

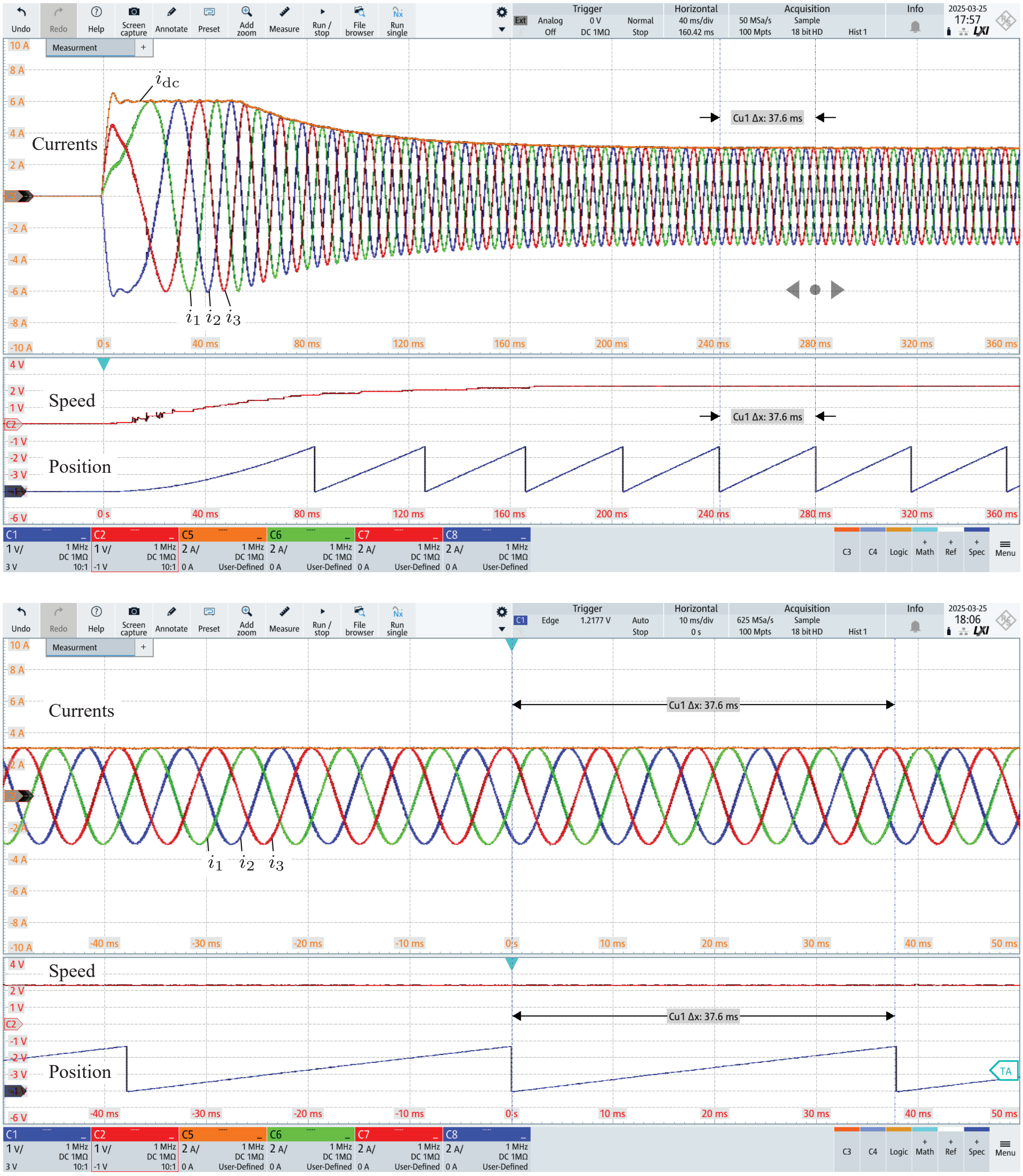

Figure 11 Measurement results validating the E-DCM concept: **(a)** Start-up transient showing the E-DCM drive system accelerating from standstill to 1600 rpm, and **(b)** steady-state operation at 1600 rpm.

and therefore no equivalent DC-side back EMF to oppose the applied voltage. As the drive accelerates, the back EMF increases, causing the DC current to decrease until it stabilizes at its steady-state value required to drive the load.

The resulting input power is approximately $10.8\,\mathrm{V} \cdot 3\,\mathrm{A} = 32.5\,\mathrm{W}$, which is well below the target power level of 5 kW (see **Tab. 1**), but it effectively demonstrates the E-DCM concept. The corresponding steady-state operation at this reduced power level is shown in **Fig. 11(b)**. The position signal is obtained from the encoder, while the speed is derived by differentiating the position, which introduces visible noise on the speed waveform. Both signals are converted to analog voltages using DACs and measured using an oscilloscope. The PMSM used in the setup has 4 pole pairs, which can be verified by observing the current waveform, showing four electrical periods within one mechanical revolution.

7. Conclusions

This paper focuses on a CSI drive system with an input buck stage that controls the DC link current and a second CSI stage that supplies the PMSM. Conventionally, achieving speed control in such systems requires the user to set a DC current reference and manage the PMSM speed and torque control through field control using the CSI. In this paper, we propose a method to simplify such drive systems by operating the CSI in an open loop with a fixed modulation index. This approach allows the user to control the speed and torque of the PMSM directly through the input converter, where, under the open-loop operation of the CSI, the PMSM torque is directly proportional to the DC link current. This makes the CSI behave like a DC machine from the user's perspective, simplifying operation and control and enabling broader and easier adoption of CSI drive systems in the industry. We refer to this control concept as the *Equivalent DC Machine* (E-DCM) since the CSI supplying the PMSM behaves like a traditional DC machine on the DC side. Thus, the E-DCM concept combines the simplicity of a DC machine with the advantages of a PMSM, such as higher torque/power density and lower maintenance.

To validate this concept, we provided analytical derivations of the CSI's DC side equivalent circuit and developed the equivalent steady-state speed-torque characteristics. We then verified these characteristics and implemented a speed control for a 5 kW CSI-supplied PMSM, where the E-DCM concept was tested by accelerating the PMSM from zero to its nominal speed of 3000 rpm. The results demonstrated a speed transient response, with the PMSM's AC current peaks precisely tracking the DC link current, as expected for the E-DCM concept.

Our future work will focus on extending the operating range of the E-DCM concept to cover a wider range of speeds, which requires m and θ_i to be functions of mechanical speed Ω. Furthermore, the E-DCM concept for interior PMSMs will be considered.

References

(1) S. Mirić, P. Pejović, T. Ohno, and M. Haider, "Current source inverter drive system with equivalent DC-machine control characteristics," in *Proc. of 27th International Conference on Electrical Machines and Systems (ICEMS2024-Fukuoka)*. Fukuoka, Japan: IEEJ, 2024.

(2) K. Imai, S. Doki, K. Kondo, and Y. Aoki, "Extended emf observer of dual three-phase permanent magnet synchronous motor operable in overmodulation drive," *IEEJ Journal of Industry Applications*, vol. 12, no. 5, pp. 901–913, 2023.

(3) H.-W. Lee, J.-H. Hwang, and K.-B. Lee, "Simplified deadbeat predictive torque control based on discrete space vector modulation for driving an open-end winding permanent magnet synchronous motor," *IEEJ Journal of Industry Applications*, vol. 13, no. 3, pp. 308–316, 2024.

(4) V. Madonna, G. Migliazza, P. Giangrande, E. Lorenzani, G. Buticchi, and M. Galea, "The rebirth of the current source inverter: Advantages for aerospace motor design," *IEEE Industrial Electronics Magazine*, vol. 13, no. 4, pp. 65–76, 2019.

(5) Y. Miyama, M. Hazeyama, S. Hanioka, N. Watanabe, A. Daikoku, and M. Inoue, "PWM carrier harmonic iron loss reduction technique of permanent-magnet motors for electric vehicles," *IEEE Transactions on Industry Applications*, vol. 52, no. 4, pp. 2865–2871, 2016.

(6) J. M. Erdman, R. J. Kerkman, D. W. Schlegel, and G. L. Skibinski, "Effect of PWM inverters on AC motor bearing currents and shaft voltages," *IEEE transactions on Industry Applications*, vol. 32, no. 2, pp. 250–259, 1996.

(7) G. L. Skibinski, R. J. Kerkman, and D. Schlegel, "EMI emissions of modern PWM AC drives," *IEEE Industry Applications Magazine*, vol. 5, no. 6, pp. 47–80, 1999.

(8) M. Kaufhold, H. Aninger, M. Berth, J. Speck, and M. Eberhardt, "Electrical stress and failure mechanism of the winding insulation in PWM-inverter-fed low-voltage induction motors," *IEEE Transactions on industrial electronics*, vol. 47, no. 2, pp. 396–402, 2000.

(9) M. Haider, M. Guacci, D. Bortis, J. W. Kolar, and Y. Ono, "Analysis and evaluation of active/hybrid/passive dv/dt-filter concepts for next generation SiC-based variable speed drive inverter systems," in *Proc. of IEEE Energy Conversion Congress and Exposition (ECCE-2020)*. Detroit, MI, USA: IEEE, 2020, pp. 4923–4930.

(10) K. Shirabe, M. M. Swamy, J.-K. Kang, M. Hisatsune, Y. Wu, D. Kebort, and J. Honea, "Efficiency comparison between Si-IGBT-based drive and GaN-based drive," *IEEE Transactions on Industry Applications*, vol. 50, no. 1, pp. 566–572, 2013.

(11) F. Maislinger, H. Ertl, G. Stojcic, C. Lagler, and F. Holzner, "Design of a 100 khz wide bandgap inverter for motor applications with active damped sine wave filter," *The Journal of Engineering*, vol. 2019, no. 17, pp. 3766–3771, 2019.

(12) V. Madonna, P. Giangrande, W. Zhao, H. Zhang, C. Gerada, and M. Galea, "On the design of partial discharge-free low voltage electrical machines," in *Proc. of IEEE International Electric Machines & Drives Conference (IEMDC-2019)*. San Diego, CA, USA: IEEE, 2019, pp. 1837–1842.

(13) M. Antivachis, D. Bortis, D. Menzi, and J. W. Kolar, "Comparative evaluation of Y-inverter against three-phase two-stage buck-boost DC-AC converter systems," in *Proc. of IEEE International Power Electronics Conference (IPEC-2018, ECCE Asia)*. Niigata, Japan: IEEE, 2018, pp. 181–189.

(14) R. A. Torres, H. Dai, W. Lee, B. Sarlioglu, and T. Jahns, "Current-source inverter integrated motor drives using dual-gate four-quadrant wide-bandgap power switches," *IEEE Transactions on Industry Applications*, vol. 57, no. 5, pp. 5183–5198, 2021.

(15) J. Huber and J. W. Kolar, "Monolithic bidirectional power transistors," *IEEE Power Electronics Magazine*, vol. 10, no. 1, pp. 28–38, 2023.

(16) N. Nain, J. Huber, and J. W. Kolar, "Comparative evaluation of three-phase ac-ac voltage/current-source converter systems employing latest gan power transistor technology," in *Proc. of International Power Electronics Conference (IPEC-2022, ECCE Asia)*. Himeji, Japan: IEEE, 2022, pp. 1726–1733.

(17) G. Migliazza, G. Buticchi, E. Carfagna, E. Lorenzani, V. Madonna, P. Giangrande, and M. Galea, "DC current control for a single-stage current source inverter in motor drive application," *IEEE Transactions on Power Electronics*, vol. 36, no. 3, pp. 3367–3376, 2020.

(18) Plexim GmbH, *PLECS: The Piecewise Linear Electrical Circuit Simulation Software*, Plexim GmbH, Zurich, Switzerland, 2024, version 4.6, accessed December 2024. [Online]. Available: https://www.plexim.com

(19) S.-H. Kim, *Electric motor control: DC, AC, and BLDC motors*. Elsevier,

2017.

(20) Teknic, Inc., "M-2310p-ln-04k permanent magnet servo motor datasheet," https://www.teknic.com, 2024, available at: https://www.teknic.com/files/product-info/N23_Industrial_Grade_Motors_v6.3.pdf.

(21) P. Pejović, T. Ohno, U. Borović, and S. Mirić, "Pulse width modulation for current source inverters with arbitrary number of phases," *Scientific Reports*, vol. 15, no. 1, p. 8744, 2025.

Appendix

1. DC Machine Voltage-Speed Transfer Function

This appendix provides the derivation of the transfer function for a DC machine (DCM) from the input armature voltage to the mechanical speed at the shaft. The derivation begins with (17), expressed in the time domain, which is then transformed into the Laplace domain. In this domain, the quantities are represented as $\overline{u}_{\mathrm{a}}(t) \rightarrow U_{\mathrm{a}}(s)$ and $i_{\mathrm{dc}}(t) \rightarrow I_{\mathrm{dc}}(s)$. Thus, (17) can be rewritten as:

$$U_{\mathrm{a}}(s) = (R_{\mathrm{a}} + sL_{\mathrm{a}})I_{\mathrm{dc}}(s) + k_{\mathrm{T}}\Omega(s), \quad \text{(A1)}$$

where s represents the Laplace domain operator. The armature resistance is given by $R_{\mathrm{a}} = R_{\mathrm{dc}} + R_{\mathrm{x}} = R_{\mathrm{dc}}$, since $R_{\mathrm{x}} = 0$ due to the constant modulation index of the E-DCM ($m = M = 1$), as shown in (14). The armature inductance in (A1) is defined as $L_{\mathrm{a}} = L_{\mathrm{f}} + L_{\mathrm{dc}}$. The back EMF term in (A1) is derived in (25). Considering the values of M and θ_I for the E-DCM (see (32)), the back EMF is expressed as $E_{\mathrm{dc}} = k_{\mathrm{T}}\Omega(s)$.

The moment of inertia J of the PMSM relates the torque to the shaft speed as:

$$T(s) = sJ\Omega(s), \quad \text{(A2)}$$

where the torque for the E-DCM is also expressed as $T(s) = k_{\mathrm{T}} I_{\mathrm{dc}}(s)$. Combining these, the DC link current can be written as:

$$I_{\mathrm{dc}}(s) = \frac{sJ\Omega(s)}{k_{\mathrm{T}}}. \quad \text{(A3)}$$

Substituting (A3) into (A1) yields the transfer function from armature voltage to shaft speed:

$$G_{\mathrm{u},\Omega}(s) = \frac{\Omega(s)}{U_{\mathrm{a}}(s)} = \frac{\frac{k_{\mathrm{T}}}{JL_{\mathrm{a}}}}{s^2 + \frac{R_{\mathrm{a}}}{L_{\mathrm{a}}}s + \frac{k_{\mathrm{T}}^2}{JL_{\mathrm{a}}}}, \quad \text{(A4)}$$

which represents a second-order transfer function.

Spasoje Mirić (Non-member) received his B.Sc., M.Sc., and Ph.D. in electrical engineering from the University of Belgrade, School of Electrical Engineering, in 2012, 2013, and 2018, respectively, focusing on power electronics systems and drives. In 2021, he defended his second Ph.D. thesis at ETH Zurich, specializing in advanced mechatronic systems. His research during this Ph.D. centered on linear-rotary actuator systems with magnetic bearings, resulting in two new machine topologies that have been patented. Since 2021, Dr. Miric has been a postdoctoral researcher at ETH Zurich, where his research included WBG power converter optimization with both hard and soft-switching, wireless power transfer systems, and eddy-current-based position sensor systems. In 2023, Dr. Miric was appointed Assistant Professor and Head of the Innsbruck Drives and Energy Systems Laboratory at the University of Innsbruck (UIBK). Dr. Miric has authored over 40 scientific papers in international journals and conference proceedings and holds seven patents. He has presented three educational seminars at leading international conferences and has received five IEEE Transactions and Conference Prize Paper Awards.

Predrag Pejović (Non-member) was born in Belgrade, Serbia, in 1966. He received the B.S. and M.S. degrees in electrical engineering from the University of Belgrade, Belgrade, in 1990 and 1992, respectively, and Ph.D. degree from the University of Colorado, Boulder, CO, USA, in 1995. In 1995, he rejoined the University of Belgrade, where he is currently a Professor in charge of teaching electrical measurements, software tools in electronics, analog electronics, and four courses in power electronics. His research interests include analog circuit design, three-phase high-power-factor rectifiers, dynamics of nonlinear systems, electronics measurements, automated measurement systems, wireless positioning, techniques for computer-aided analysis, and optimization of power electronic systems.

Takanobu Ohno (Member) received his B.Sc., M.Sc., and Ph.D. in electrical engineering from Tokyo University of Science, Japan, in 2018, 2020, and 2022, respectively. From 2022 to 2023, he was a visiting researcher with Power Electronic Systems Laboratory, Swiss Federal Institute of Technology (ETH) Zurich, Switzerland. In 2023, he joined Innsbruck Drives and Energy Systems Laboratory at the University of Innsbruck, Austria, where he is currently a Postdoctoral Researcher with the Department of Mechatronics. His research interests include control and modulation for power electronics and drive systems.

Michael Haider (Non-member) received his M.Sc. and Ph.D. in electrical engineering from the Swiss Federal Institute of Technology (ETH) Zurich, Switzerland, in 2017 and 2022, respectively. In 2017, he joined the Power Electronic Systems Laboratory, ETH Zurich, as a Ph.D. student, focusing on motor-integrated power factor corrected single-to-three- phase AC/AC converter concepts. His research interests include synergetically controlled two-stage systems, soft-switching converter topologies, wide-bandgap power semiconductor devices, and their application in next-generation variable speed drive systems.